

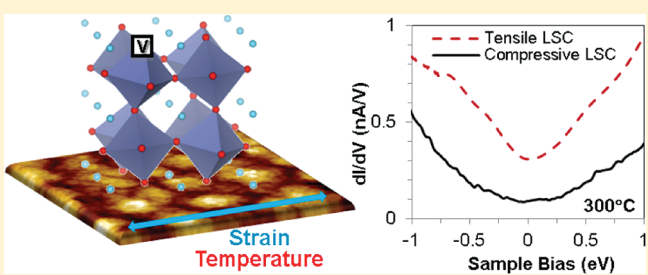
Surface Electronic Structure Transitions at High Temperature on Perovskite Oxides: The Case of Strained $\text{La}_{0.8}\text{Sr}_{0.2}\text{CoO}_3$ Thin Films

Zhuhua Cai,[†] Yener Kuru,^{†,‡} Jeong Woo Han,[†] Yan Chen,[†] and Bilge Yildiz*,[†]

[†]Laboratory for Electrochemical Interfaces, Department of Nuclear Science and Engineering, and [‡]Department of Material Science and Engineering, Massachusetts Institute of Technology, 77 Massachusetts Avenue, Cambridge, Massachusetts 02139, United States

Supporting Information

ABSTRACT: In-depth probing of the surface electronic structure on solid oxide fuel cell (SOFC) cathodes, considering the effects of high temperature, oxygen pressure, and material strain state, is essential toward advancing our understanding of the oxygen reduction activity on them. Here, we report the surface structure, chemical state, and electronic structure of a model transition metal perovskite oxide system, strained $\text{La}_{0.8}\text{Sr}_{0.2}\text{CoO}_3$ (LSC) thin films, as a function of temperature up to 450 °C in oxygen partial pressure of 10^{-3} mbar. Both the tensile and the compressively strained LSC film surfaces transition from a semiconducting state with an energy gap of 0.8–1.5 eV at room temperature to a metallic-like state with no energy gap at 200–300 °C, as identified by *in situ* scanning tunneling spectroscopy. The tensile strained LSC surface exhibits a more enhanced electronic density of states (DOS) near the Fermi level following this transition, indicating a more highly active surface for electron transfer in oxygen reduction. The transition to the metallic-like state and the relatively more enhanced DOS on the tensile strained LSC at elevated temperatures result from the formation of oxygen vacancy defects, as supported by both our X-ray photoelectron spectroscopy measurements and density functional theory calculations. The reversibility of the semiconducting-to-metallic transitions of the electronic structure discovered here, coupled to the strain state and temperature, underscores the necessity of *in situ* investigations on SOFC cathode material surfaces.



1. INTRODUCTION

The slow rate of oxygen reduction (OR) at the cathode is considered to be the main barrier for implementation of high performance solid oxide fuel cell (SOFC) systems at intermediate temperatures (500–700 °C).^{1–4} Surface oxygen exchange is the key process that limits the OR kinetics on the mixed ionic and electronic conducting cathodes. The kinetics of oxygen exchange on the surface depends on the electronic structure and surface chemistry (i.e., cation concentration and oxygen nonstoichiometry) driven by temperature and oxygen partial pressure.^{5–7} In addition to the temperature and oxygen partial pressure, there is evidence from recent literature that lattice strain may also serve as a thermodynamic and kinetic driving force for the surface exchange and diffusion of oxygen ions, by influencing the interface cation chemistry,^{8–11} surface oxygen stoichiometry,¹² electrical conductivity,¹³ and surface and bulk ionic transport.^{14–17} The strong coupling between the biaxial strain to the ionic conductivity has been first shown in the fluorite structured SOFC electrolyte material Y_2O_3 -stabilized ZrO_2 (YSZ),^{14–16,18} suggesting the possibility of a significantly enhanced strain-driven ionic conductivity due to reduced migration energy barriers. However, *in situ* studies of how the key descriptors of OR activity evolve with temperature, oxygen pressure, and strain state have been largely missing, except from a few recent studies.^{5–7} This is because the functional conditions of SOFC cathodes at elevated

temperatures and reactive gas pressures are too harsh for the traditional vacuum-based surface science techniques.^{19–21}

Herein we describe the temperature and strain effects on the surface of strontium-doped lanthanum cobaltite, a widely studied and promising SOFC cathode material,^{22,23} using new developments in *in situ* scanning probe-based surface science methods. We have recently demonstrated, using density functional theory (DFT) calculations, that the epitaxial tensile strain can alter the surface thermodynamics of LaCoO_3 by impacting the oxygen adsorption and oxygen vacancy formation energies.¹² Direct experiments probing the effects of strain on the surface of the LaCoO_3 have yet been missing. The markedly enhanced oxygen exchange rates on Sase et al.'s $\text{La}_{0.6}\text{Sr}_{0.4}\text{CoO}_3$ / $(\text{La},\text{Sr})_2\text{CoO}_4$ heterointerface system²⁴ and on La O' et al.'s $\text{La}_{0.8}\text{Sr}_{0.2}\text{CoO}_3$ thin films²⁵ could potentially be explained by the driving role of lattice strain in oxygen vacancy formation.^{12,26} These recent examples together motivate our investigation of the surface chemical state and electronic structure of LSC as a model system, not only as a function of temperature but also as a function of epitaxial lattice strain, in connection to surface reactivity with oxygen. Furthermore, the impact of lattice strain on the surface electronic structure and reactivity has been long demonstrated for

Received: June 26, 2011

Published: September 14, 2011

low-temperature transition metal electrocatalysts.^{27–29} The relation is explained on the basis of the center of the metal d-band electronic states and the modified degree of hybridization of the transition metal d-band and the adsorbed oxygen 2p electronic states (for the case of oxygen adsorption and dissociation). On transition metal perovskite oxides, however, the processes that describe “reactivity” are associated with two cation sublattices and an anion sublattice, which are more complex and not nearly well explored compared to the transition metal surfaces. On the basis of the motivating evidence summarized above, a direct mechanistic understanding of the strain-driven chemical and electronic states on transition metal oxide cathode surfaces for accelerating OR kinetics is needed.

In this study, we probed the impact of temperature and lattice strain on the surface electronic structure and the chemical state as important determinants of oxygen reduction activity on epitaxial LSC films as a model system. Both the tensile and the compressive strained LSC film surfaces transition from a semiconducting state at room temperature to a metallic-like state at elevated temperatures, as captured by *in situ* scanning tunneling microscopy and spectroscopy (STM, STS). The tensile strained LSC surface exhibits a more enhanced electronic DOS near the Fermi level following this transition, indicating a more highly active surface for electron transfer. We hypothesize that the governing reason for the enhanced DOS on the tensile strained LSC is the easier formation of oxygen vacancy defects when LSC is tensile strained. This hypothesis is supported by both our X-ray photoelectron spectroscopy (XPS) results and our DFT calculations of oxygen vacancy formation energies. The results represent an initial set of *in situ* correlations of chemical and electronic state to the temperature and strain state together on dense thin film perovskite cathodes, which are not possible to capture by *ex situ* measurement alone. The organization of the rest of this paper is as follows. In section 2, the experimental methods and simulation details are described. In section 3, experimental results on the temperature-dependent surface chemistry and electronic structure are presented, accompanied with discussion about their physical meaning and significance. Finally in section 4, we summarize our major observations and conclusions.

2. METHODS

LSC films with thicknesses of ~20 nm on single crystal SrTiO₃ (STO) and LaAlO₃ (LAO) were fabricated by pulsed laser deposition (PLD), using a KrF excimer laser at a wavelength of 248 nm. Laser beam energy was set at 550 mJ per pulse at 10 Hz pulse frequency. The optimum growth conditions for these epitaxial films were at 750 °C with O₂ pressure (P_{O_2}) of 20 mTorr, with the substrate located at a distance of 6.0 cm away from target. After deposition, the sample was cooled at 10 °C/min to room temperature under a P_{O_2} of 10 Torr.

Ex situ X-ray diffraction (XRD) 2θ–ω scans, X-ray reflectivity (XRR) measurements, and *in situ* reciprocal space mapping (RSM) were performed to characterize the crystal structure, thickness, and strain states, respectively, of the LSC films. RSM was performed both at room temperature and at 500 °C in air. The measurements employed a high-resolution four-circle Bruker D8 Discover diffractometer, equipped with a Göbel mirror, four-bounce Ge(002) channel-cut monochromator, Eulerian cradle, and a scintillation counter, using Cu Kα₁ radiation.

In situ X-ray photoelectron spectroscopy was used to identify the surface cation chemistries as a function of temperature. The Omicron EA 125 hemispherical analyzer and Omicron DAR 400 Mg/Al dual anode nonmonochromated X-ray source were used for XPS measurements, and CasaXPS 2.3.15 software was used for peak fitting and

quantification (See Supporting Information for peak fitting details). Carbon contamination was removed from the surfaces of the air-exposed LSC films by heating them in an oxygen pressure of 10⁻⁴ mbar at 450 °C for 1.5 h in the UHV chamber. Spectra were acquired over 25–450 °C and at 10⁻⁹ mbar with emission angles from 0° to 60° as defined relative to the surface normal plane. The Sr 3d, La 3d, and Co 2p emissions were measured and used in the analysis. For the excitation energy of 1253.6 eV, the sampling depths of these photoelectrons at 0° emission angle are ~6 nm for Sr 3d, ~3 nm for La 3d, and ~3 nm for Co 2p.³⁰ At the emission angle of 60°, the measurements are more surface sensitive, since the sampling depths of each element are half of those at the emission angle of 0°.

High spatial resolution probing of the surface morphology and electronic structure was achieved by using a modified variable-temperature scanning tunneling microscope by Omicron GmbH from room temperature up to 450 °C in 10⁻³ mbar oxygen. STM was performed in the constant-current mode using Pt/Ir tips, with a sample bias voltage of 2 V and a feedback tunneling current of 200–500 pA. A retractable oxygen doser was used for directly exposing the surface with oxygen during imaging and tunneling spectroscopy measurements.

Because our experimental results on the surface electronic structure at elevated temperatures were interpreted on the basis of the role of oxygen vacancies, we assessed the oxygen vacancy formation on the LSC surface using first-principles based calculations in the framework of DFT. The generalized gradient approximation (GGA) parametrized by Perdew and Wang³¹ along with the projector augmented wave (PAW) method³² was used to describe ionic cores. To avoid the self-interaction errors that occur in the traditional DFT for strongly correlated electronic systems, the DFT+U method accounting for the on-site Coulomb interaction in the localized d or f orbitals was adopted, with an effective $U-J = 3.3$ eV that was previously used accurately for LaCoO₃.^{33–35} All calculations used a plane wave expansion cutoff of 400 eV and included spin polarization. Further computational details of the model can be found in our recent reports.^{12,35,36} Oxygen vacancy formation energy is calculated as^{37,38}

$$E_{\text{vac}} = \frac{1}{2} \{ E_{\text{surf/vac}} - E_{\text{surf/bare}} \} + \mu_O(T, P_{O_2}) \quad (1)$$

where E_{vac} is oxygen vacancy formation energy, $E_{\text{surf/vac}}$ is the total energy of a symmetric slab with a vacancy on both surfaces of the slab, $E_{\text{surf/bare}}$ is the total energy of a slab without a vacancy, and $\mu_O(T, P_{O_2})$ is the chemical potential of oxygen in the gas phase (O atoms in O₂ molecules). The oxygen vacancy formation energy we calculated here is for the removal of a neutral oxygen atom from the lattice. The chemical potential term depends on temperature and pressure and is typically taken from experimental data.³⁹ At 0 K, the vacancy formation energy corresponds to enthalpy of formation with the $\mu_O(T, P_{O_2})$ equal to half of the DFT-calculated total energy of an isolated O₂ molecule.

3. RESULTS AND DISCUSSION

3.1. Structure of the Strained LSC Films. The bulk crystal of the perovskite LSC has a rhombohedral unit cell, $a = b = 5.447$ Å, $c = 13.178$ Å, which is related to the average perovskite structure with a pseudocubic lattice constant of a_{pc} (b_{pc}) = 3.851 Å. Two different single-crystal substrates SrTiO₃ (100) (STO, $a = 3.905$ Å) and LaAlO₃ (100) (LAO, $a = 3.793$ Å) were used to produce a 1.4% tensile and –1.5% compressive strain within the pseudocubic LSC, respectively, at room temperature. At the experimental temperature of up to 450 °C and the growth temperature of 750 °C, the expected tensile strains induced by STO decrease to 1.0% and 0.7%, respectively, while the compressive strains induced by LAO increase to –1.9% and –2.2%, respectively, due

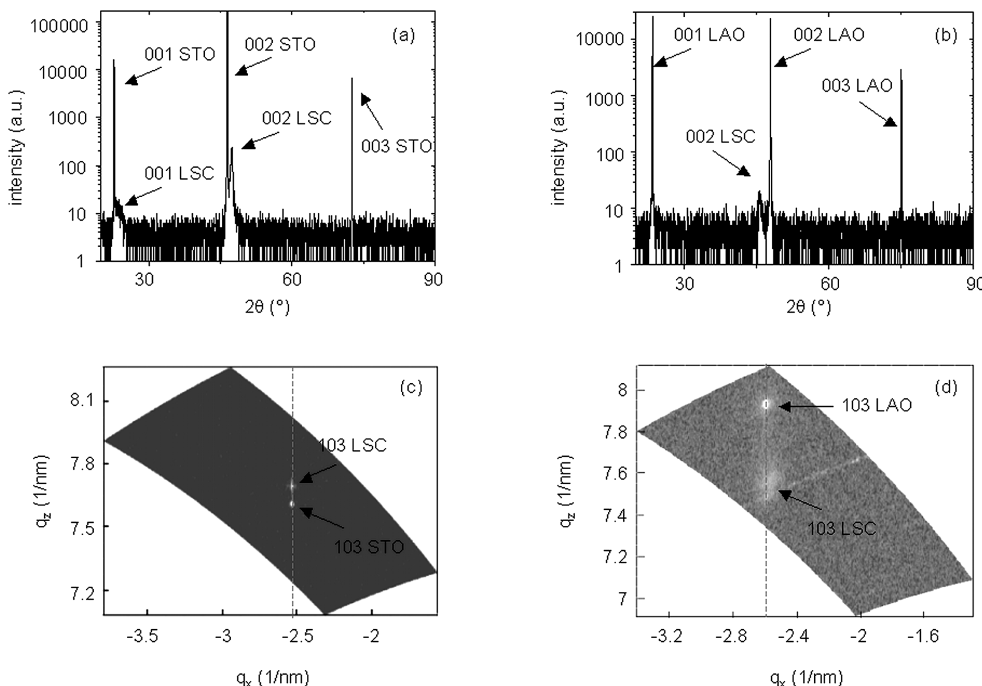


Figure 1. The $2\theta - \omega$ scans in logarithmic intensity scale of (a) LSC/STO and (b) LSC/LAO show only $h00$ diffraction peaks of LSC. X-ray diffraction reciprocal space maps were measured at $500\text{ }^{\circ}\text{C}$ for (c) LSC/STO and (d) LSC/LAO thin films. The arrows in parts c and d show the 103 reflections of the LSC thin films and the substrates. The dashed vertical lines in parts c and d indicate that the average in-plane lattice parameters of both films match the in-plane lattice parameters of their substrates, which confirms fully strained LSC films at $500\text{ }^{\circ}\text{C}$ (the same signature as those measured at room temperature in Figure S1 of the Supporting Information).

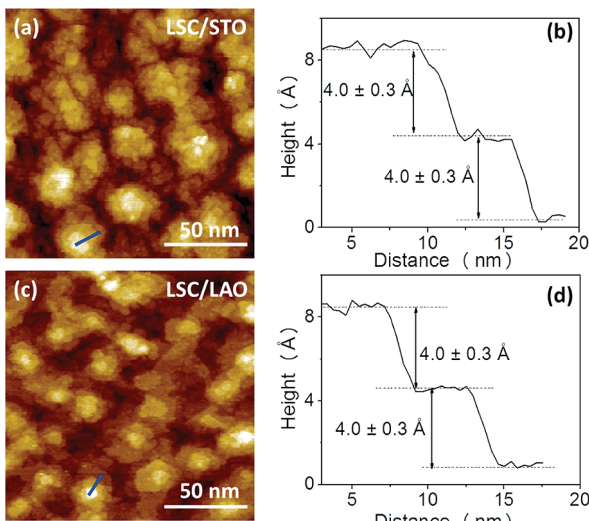


Figure 2. LSC surface morphology on (a) STO and (c) LAO showed layered structures at room temperature, imaged by scanning tunneling microscopy. Height profiles of (b) LSC/STO and (d) LSC/LAO showed a step height of $4.0 \pm 0.3\text{ \AA}$, which matches well the LSC lattice constant (3.85 \AA). Blue bars in parts a and c show the position of the line profiles in parts b and d.

to the different thermal expansion coefficients of the film and the substrates.

XRD $2\theta - \omega$ scans (Figure 1a,b) of the as-deposited LSC films grown on both substrates, hereafter denoted as LSC/LAO and LSC/STO, exhibited only $h00$ diffraction peaks, indicating that single-phase LSC layers were successfully grown on both substrates,

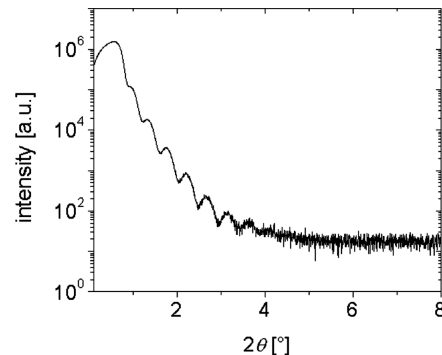


Figure 3. X-ray reflectivity data measured on LSC/STO show the presence of well-defined Kiessig fringes that demonstrate the structural coherence of the film.

with the $h00$ planes of the films parallel to the substrate surfaces. XRD reciprocal space maps measured at $500\text{ }^{\circ}\text{C}$ in air around the 103 Bragg reflection of the pseudocubic LSC thin films (Figure 1c,d) confirm that the LSC film is fully strained by the STO substrate, since the in-plane components of the reciprocal lattice vectors for both the film and the substrate are exactly matching. The in-plane components of the reciprocal lattice vectors are nearly identical also for the LSC film deposited on LAO substrate. However, the 103 reflection of the LSC film on LAO substrate is more diffuse compared to the film on STO, which may stem from a strain gradient through the film thickness, the presence of a defective structure in the substrate, small crystallite size, and lattice imperfections in combination with slight changes in the orientation of the diffraction vector for different

crystallites. (At room temperature, both films also show fully strained coherence with the substrates. See Figure S1 of the Supporting Information.)

The surface of the LSC films grown on STO and LAO has well-resolved, atomically smooth terraces (Figure 2a,c), indicating a layered structure with an overall root-mean-square roughness of less than 1 nm. The height difference of 4.0 ± 0.3 Å between each layer (Figure 2b,d) is consistent with the lattice parameter (3.85 Å) of the LSC. The continuity of these films was confirmed by XRR measurement, which showed well-defined finite-size peaks, the Kiessig fringes (Figure 3). The presence of these well-defined fringes demonstrates the structural coherence between the top of the film and the film/substrate interface. From the analysis of the XRR peaks, the thickness and surface roughness of the films were found to be 19 nm and about 1 nm, respectively. The color-contrast shown in the STM images for both films (Figure 2a,c) corresponds to a peak-to-valley height difference of only 1–2 nm, consistent with the XRR results. The layer-by-layer nature of the surfaces of these two sets of films is similar to each other, enabling a comparison between them that may have only minimal (if any) artifacts due to morphology differences.

3.2. Surface Chemistry of the Strained LSC Films at Room Temperature. The Sr content on the A-site [quantified as $\text{Sr}/(\text{Sr} + \text{La})$] and the relative presence of A-site versus B-site cations [quantified as $(\text{Sr} + \text{La})/\text{Co}$] on the LSC surface were assessed by analyzing the Sr 3d, La 3d, and Co 2p emissions in the angle-resolved XPS measurements. At the emission angle of 60°, the $(\text{Sr} + \text{La})/\text{Co}$ ratios on the surface of LSC/STO and LSC/LAO are 3.02 ± 0.15 and 2.64 ± 0.10 , respectively, which suggest primarily AO-terminated surfaces ($\text{A} = \text{La}, \text{Sr}$). The $\text{Sr}/(\text{Sr} + \text{La})$ ratios at 60° of 0.44 ± 0.02 and 0.41 ± 0.02 found for LSC/STO and LSC/LAO, respectively, show an enhanced presence of Sr cations on the A-site on both of the LSC film surfaces. The bulk composition of a thick (~400 nm thick) LSC film was found by energy dispersive X-ray spectroscopy (EDS), showing that the $\text{Sr}/(\text{Sr} + \text{La})$ is 0.21 ± 0.02 and the $(\text{La} + \text{Sr})/\text{Co}$ is 0.93 ± 0.05 . The bulk film composition determined by EDS is nearly the nominal stoichiometry, considering the quantification accuracy of 4–5% for EDS.⁴⁰ This confirms that the surface compositions that are rich in Sr and in A-site cations identified by XPS are not artifacts of PLD throughout the film. Furthermore, the surface and subsurface contributions to the Sr 3d spectra, namely, the $\text{Sr}_{\text{surface}}$ and $\text{Sr}_{\text{lattice}}$, were identified. We use the $\text{Sr}_{\text{surface}}/\text{Sr}_{\text{lattice}}$ ratio as another measure of the segregation tendency of Sr on the perovskite surface (see Figure S2 of the Supporting Information for detailed analysis). The $\text{Sr}_{\text{surface}}/\text{Sr}_{\text{lattice}}$ on the tensile strained LSC/STO is 1.3, larger than 1.1 on the compressively strained LSC/LAO. The enhanced presence of the $\text{Sr}_{\text{surface}}$ and the larger $\text{Sr}/(\text{Sr} + \text{La})$ ratio on LSC/STO suggest a small further enrichment of surface Sr driven by the tensile strain state of the LSC film.³⁶ It is not only the composition but also, and perhaps more importantly so, the atomic structure of the surface that is important in determining the surface electronic structure and reactivity. When Sr enriches on the LSC, the surface can evolve and form different atomic structures. In the simplest case, Sr replaces La on the surface^{7,36} while retaining a perovskite-terminated structure. Surface phase separations in the form of SrO ^{41,42} and Ruddlesden–Popper (RP) phases, for example $(\text{La}, \text{Sr})_2\text{MnO}_4$ on $(\text{La}, \text{Sr})\text{MnO}_3$ ⁴³ are also possible. Each of these phases has a characteristic and distinct lattice parameter that should reflect as step height difference on the surface. Our STM images (Figure 2a,c) showed that

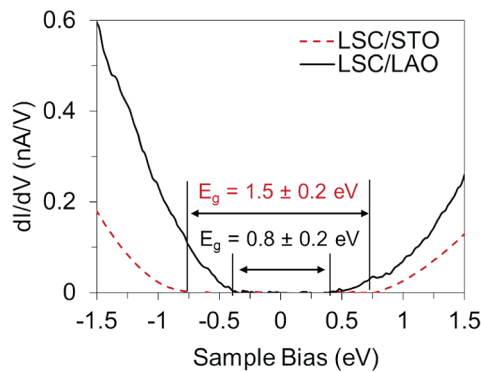


Figure 4. Tunneling spectra (dI/dV) taken at room temperature, representing the surface occupied and unoccupied electronic states in the electronic structure near the Fermi level (0 eV) on LSC/STO and LSC/LAO; the tensile strained LSC/STO has a larger energy gap (E_g) than the compressively strained LSC/LAO.

the step height difference matches well with the perovskite LSC lattice constant. This information combined with the XPS result discussed above suggests that the LSC surfaces reported here retain a perovskite-like structure and are terminated with the AO-layer on which Sr replaces La to a greater extent than the bulk nominal Sr-content. No evidence for the presence of SrO or RP phases was found on the surface. However, since we could not obtain atomic resolution laterally on these surfaces, we cannot eliminate the possibility of lateral surface reconstructions.

3.3. Surface Electronic Structure of the Strained LSC Films at Room Temperature. The surface reactivity of a material is governed by its electronic structure.^{28,44–47} Tunneling spectroscopy measurements to identify the surface electronic structure of the differently strained LSC films were performed as a function of temperature *in situ* from room temperature up to 450 °C in 10^{-3} mbar oxygen pressure. At room temperature LSC surfaces exhibited an energy gap between the occupied and unoccupied states (Figure 4), favoring a narrower gap (0.8 ± 0.2 eV) for the compressively strained LSC film than the tensile strained LSC film (1.5 ± 0.2 eV). The semiconducting behavior of LSC/LAO and LSC/STO surface at room temperature is contrary to the reported bulk electronic properties of $\text{La}_{1-x}\text{Sr}_x\text{CoO}_3$. Mineshige et al.⁴⁸ showed that $\text{La}_{1-x}\text{Sr}_x\text{CoO}_3$ has an insulator-to-metal transition for $x \geq 0.25$ at room temperature. STM/STS is a surface analysis tool, and our LSC thin films with $x \sim 0.4$ on the top 2–3 nm of surface exhibit a semiconducting instead of a metallic structure, suggesting a different behavior of surface states compared to the bulk LSC behavior. Rata et al. demonstrated that a strain-induced cooperative Jahn–Teller-type (JT) deformation of the CoO_6 octahedra may provide a localization mechanism in tensile LSC films on STO substrates, and thus, induce an insulating state.¹³ This cooperative JT distortion has also been reported as an efficient localization mechanism for the e_g electrons in ferromagnetic manganites.^{49–53} Furthermore, our recent DFT calculations on $\text{La}_{0.7}\text{Sr}_{0.3}\text{MnO}_3$ (LSM) showed that the lattice strain directly impacts the surface energy gap and it increases as the epitaxial strain changes from compressive to tensile.³⁶ The correlations of JT distortions and strain with the electronic structure are consistent with our tunneling spectra results here exhibiting a larger energy gap for the tensile state at room temperature. We believe that the different energy gaps on these LSC film surfaces likely arise due to a direct effect of the biaxial lattice strain on the crystal and electronic structure of LSC.

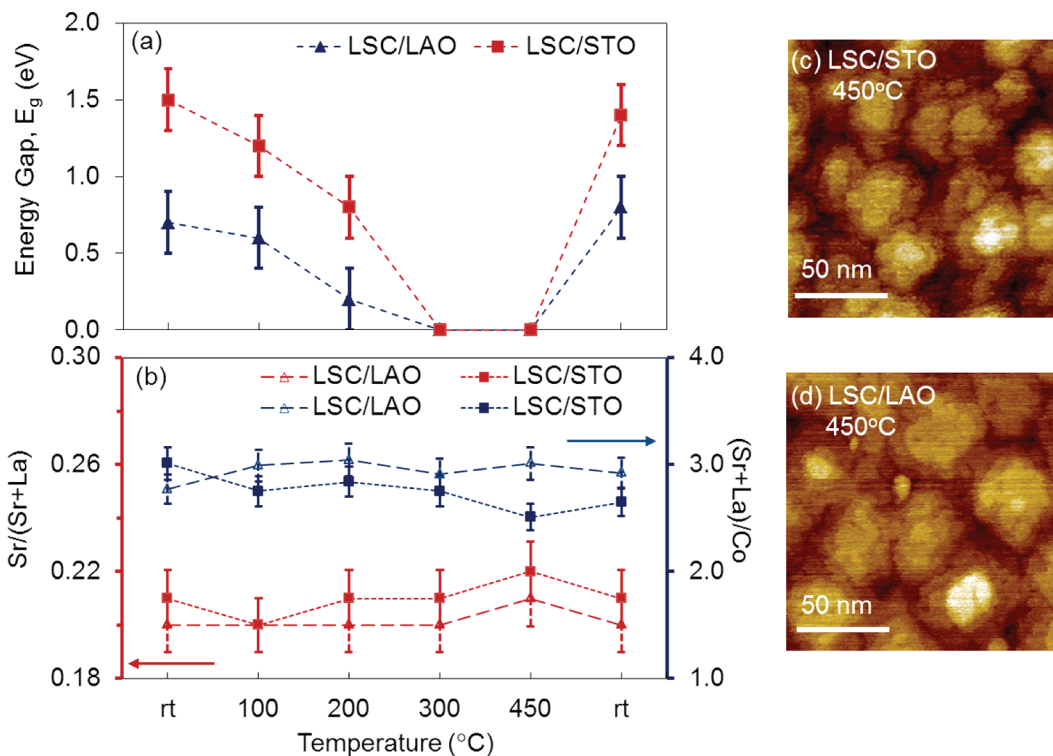


Figure 5. (a) Energy gap measured by scanning tunneling spectroscopy and (b) cation chemistries from X-ray photoelectron spectroscopy (normal emission angle) for the tensile strained LSC/STO and compressively strained LSC/LAO surface as a function of temperature from room temperature (rt) to 450 °C and back to rt. The dashed connecting lines are a guide for the eye. The surface structure of (c) LSC/STO and (d) LSC/LAO films at 450 °C shows the stability of the layered structure without evident changes in the film surface morphology.

3.4. Surface Chemistry and Electronic Structure of the Strained LSC Films at Elevated Temperatures. Investigation of how the surface electronic structure is driven by elevated temperatures is of essence to understand the electron transfer and oxygen reduction properties on SOFC cathodes, as well as in other high-temperature applications of transition metal oxides. Here we report the temperature dependence of the energy gap and electron tunneling conductance (representative of the DOS) on the surface of the tensile and compressively strained LSC films, probed *in situ* from room temperature up to 450 °C in 10⁻³ mbar of oxygen pressure. The energy gaps on both films reduce with increasing temperature, and the LSC/LAO has a smaller average surface energy gap than the LSC/STO from room temperature up to 200 °C (Figure 5a). The LSC/LAO already exhibits metallic-like regions with $E_g = 0$ eV at 200 °C, while both LSC film surfaces become entirely metallic at 300 °C. The LSC surfaces remain metallic up to 450 °C and return reversibly back to a state with the same energy gap upon cooling down to room temperature in the same oxygen pressure. This reversible transition from the presence of an energy gap to a metallic-like state in the surface electronic structure of LSC, which we name as a semiconductor-to-metal transition (SMT), is unexpected, because the thermal excitations up to 200–300 °C alone are not sufficient to enable the closure of the 0.8–1.5 eV energy gap. Furthermore, tunneling spectroscopy measurements on other perovskite surfaces^{54–57} conducted at room temperature after heating to elevated temperatures did not show such a drastic and reversible evolution in the electronic structure. Because those measurements were not performed *in situ* at the high temperatures, reversible changes in electronic structure may have been missed.

Such reversible SMTs were also observed in our recent studies of the surfaces of LSM films on LAO, STO, and YSZ^{5,36} and on the surfaces of Sr(Ti,Fe)O₃ films on YSZ⁵⁸ *in situ* at elevated temperatures (studied only at rt and at 500 °C, without a systematic identification of the intermediate transition temperatures and the cause of the transitions). We believe that the complete disappearance of the energy gap at moderately elevated temperatures is intrinsic to the LSC film surfaces here and is not an artifact of the substrates. This is because both LAO and STO are insulating under these experimental conditions,⁵⁹ and the LSC films are ~20 nm thick, which does not allow tunneling from the substrates, even if they were to become metallic. Furthermore, the morphologies of both LSC films up to 450 °C remained stable, with the same layered structure as in their initial condition (Figure 5c,d). Therefore, a bulk phase change to a metal structure does not take place in LSC under these experimental conditions.

3.5. Underlying Mechanisms of the SMT and Its Dependence on the Lattice Strain. The transition from the presence of an energy gap to a metallic-like electronic structure may arise from the formation of hole-rich regions on the surface due to Sr cation segregation at elevated temperatures,⁶⁰ as cation dynamics can take place at high temperature on oxide surfaces.⁶¹ However, the temperature at which we observe the disappearance of the energy gap is too low to enable significant cation mobility that may alter the surface cation compositions.^{5,7,62} Supporting this, XPS on both the LSC/STO and LSC/LAO (Figure 5b) did not show any evidence of surface cation movement up to the temperatures at which the transition completely took place (300 °C). Therefore, we believe that the surface cation enrichment or depletion on LSC is not responsible for the SMT that we discove-

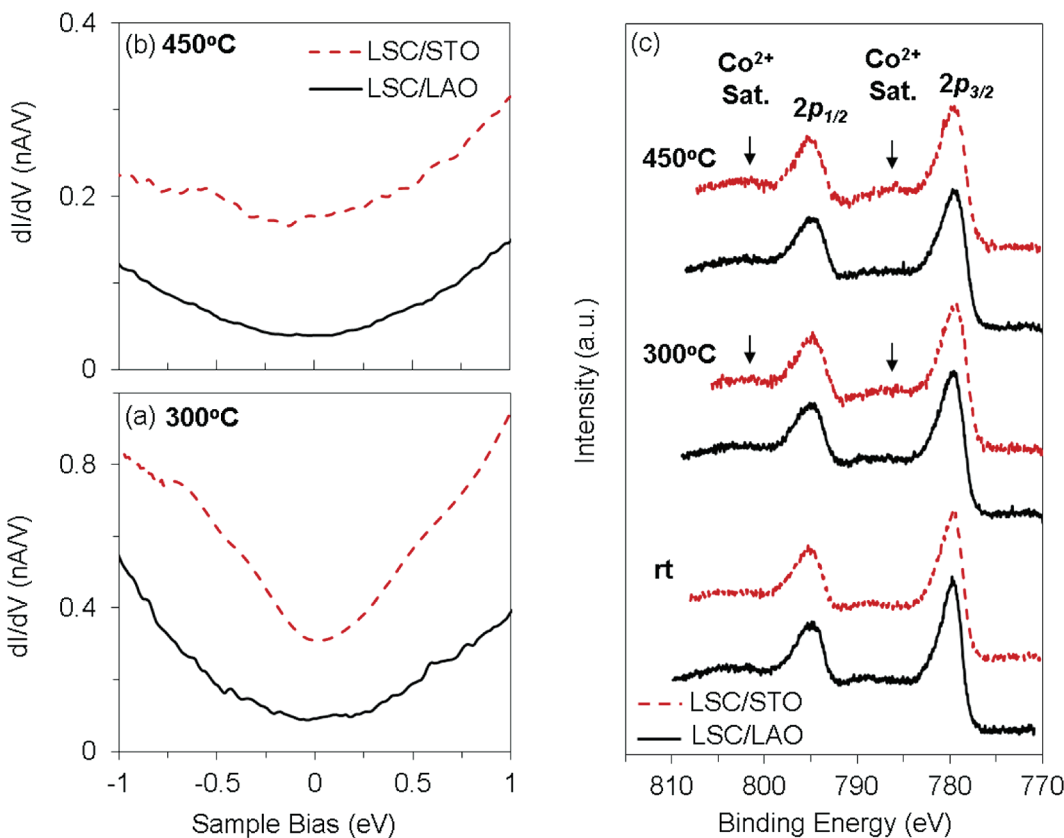


Figure 6. Tunneling spectra (dI/dV) at (a) 300 °C and (b) 450 °C, representing the DOS, and (c) Co 2p region of the photoelectron spectra on LSC/STO and LSC/LAO at 300 and 450 °C after 90 min of annealing (including the measurement time). Satellite peaks (Sat.) represent the enhanced presence of Co^{2+} oxidation state in addition to the Co^{3+} state. The Co 2p spectra show enhanced formation of Co^{2+} on the tensile strained LSC/STO films compared to the LSC/LAO at elevated temperatures.

red at 200–300 °C. Instead, the origin of the SMT on both LSC surfaces here could be attributed to the following three possible mechanisms.

The first mechanism is associated with the Co spin state transitions as a function of temperature:^{60,63} the conversion of low-spin to intermediate-spin Co ions at $T \geq 650\text{K}$ causes a transition from semiconducting to metallic state. The temperature at which the SMT on the LSC film surfaces takes place here, around 200–300 °C (473–573 K), is not too far from the temperature for the conversion of low-spin states to intermediate-spin states of cobalt ions as identified by Senaris and Goodenough.⁶³ The second mechanism is associated with the broadening of the electronic bandwidth at the elevated temperature due to structural changes that LSC undergoes. Mineshige et al.⁴⁸ identified an insulator-to-metal transition in bulk LSC with increasing temperature, which correlates well with the reducing degree of the tilting of the CoO_6 octahedra and the increasing $\text{Co}-\text{O}-\text{Co}$ angle, which broadens the bandwidths of the Co 3d and O 2p bands. When the bandwidths become larger than the charge-transfer gap, a transition to metallic state takes place, and this is at the $\text{Co}-\text{O}-\text{Co}$ angle of ca. 165°.⁴⁸ For the undoped bulk LaCoO_3 , this transition was found to take place at nearly 950 K. While this is much higher than the SMT temperature we observe here, the thin film epitaxial geometry or the Sr content may reduce the structural transition temperature, although this is not confirmed. The third mechanism is related to the formation of oxygen vacancies at elevated temperatures. The 200–300 °C temperature range is

reasonably high to initiate oxygen vacancy formation on the LSC surface, given that the vacancy formation enthalpy at 0 K on LSC surfaces is nearly 0.75 eV (lower than the vacancy formation energy of 2 eV⁶⁴ for the bulk LSC), and the free energy of formation is reduced significantly further at the experimental temperature and oxygen pressure.⁵⁷ Oxygen defects in transition metal oxides modify the d band structure of the neighboring transition metals and induce defect states in the band gap.^{65–70} Here, the enhanced oxygen vacancy defect states may interfere with the Co d band in a delocalized manner at elevated temperatures and enable the transition from the presence of an energy gap to a metallic-like state on the LSC surface. While further experimental and computational investigations are required to pin down the primary governing mechanism, we believe the oxygen vacancy defects are a more likely player for the SMT on LSC films compared to the other two mechanisms discussed above. This is in light of the following evidence on the Co oxidation state as a function of temperature and film strain state.

Furthermore, the transition to metallic state at high temperature is stronger with a larger DOS near the Fermi level for the tensile strained LSC/STO compared to the compressively strained LSC/LAO at 300 and 450 °C (Figure 6a,b). Taking the DOS near the Fermi level (0 V sample bias) as a measure of reactivity,^{46,47} our results suggest that tensile strain state on LSC may favor electron transfer to and reactivity with oxygen at elevated temperatures on cathodes of solid oxide fuel cells. This is interesting and contrary

to the room temperature state, at which the LSC/STO had a larger energy gap, emphasizing the importance of probing the surface electron transfer properties *in situ*. We note that the XPS results showed no discernible difference in the surface cation content between these two films at 300 °C and only small differences at 450 °C (Figure 5b). Furthermore, the STM images showed that the surface structure remains stable up to 450 °C (Figure 5c,d). Therefore, the possibility of cation redistribution and chemical phase separation on the surfaces can be ruled out to be responsible for the different electron transfer activities of the differently strained LSC films at elevated temperatures. We attribute the differences in the high-temperature DOS on LSC/STO and LSC/LAO to the varying ease of oxygen vacancy formation driven by strain. Strain state of the LSC films can influence the oxygen vacancy formation energies and thus the equilibrium surface vacancy concentrations at elevated temperatures.^{12,26,71} Indeed, our DFT calculations estimate a vacancy formation energy lower by 0.43 eV on the +1.0% tensile strained LaO-terminated LaCoO₃ (001) surface compared to the -1.9% compressively strained one (representative of the expected strain states of the LSC films at 450 °C). Such a significant difference in the equilibrium surface vacancy concentrations and defect configurations can influence the way the electronic structure is modified.^{72,73}

We take the Co oxidation state, observed by the Co 2p photoelectron spectra (Figure 6c), as a measure in quantifying the relative presence of surface oxygen vacancies on the LSC films. At room temperature, both film surfaces had mainly Co³⁺. This is deduced from presence of a weak satellite feature at around 790 eV that is characteristic of a mixed Co²⁺ and Co³⁺ state as in Co₃O₄,⁷⁴ and the smaller magnitude of this peak at 790 eV suggests more dominance of the Co³⁺ state. For the tensile strained LSC/STO, the Co²⁺ satellite peak^{75,76} at around 786 eV was evident already at 300 °C (upon annealing for 90 min including the measurement time), suggesting the enhanced formation of Co²⁺ due to the oxygen vacancies. At 450 °C, the Co²⁺ satellite structure on LSC/STO became more prominent, indicating the increasing formation of oxygen vacancies. In comparison, the Co 2p spectra at 300 and 450 °C for the compressively strained LSC/LAO showed a mainly Co³⁺ line shape^{74,75} without an evident Co²⁺ satellite feature for the same duration of annealing. The absence of Co²⁺ satellite peaks in the spectra from LSC/LAO may result from only a small amount of Co²⁺ formation (that our measurements were not sensitive to) or only the reduction of Co⁴⁺ to Co³⁺ that could inherently not be distinguished from the Co 2p emission by the sensitivity of the XPS technique. On the other hand, the dI/dV data on LSC/LAO shows already a complete SMT transition at those temperatures. (See the Supporting Information for the formation of Co²⁺ also on LSC/LAO only upon more prolonged annealing, and for the partial reversibility of the Co 2p spectra upon cooling down to room temperature). This suggests an easier formation of oxygen vacancies on the LSC/STO than on the LSC/LAO, consistent with our theoretical prediction of 0.43 eV lower vacancy formation energy for the tensile strained (AO-terminated) LSC surface. This difference results in a larger concentration of equilibrium oxygen defects and, we believe, governs the more highly enhanced DOS near the Fermi level for the tensile strained LSC/STO surface. Furthermore, the difference in the electronic structure as a function of the amount of vacancies shows that the vacancies not only serve as the preferred oxygen adsorption sites (as is the traditional view^{77–79}) but also enhance the electron transfer properties on the LSC surface for OR at elevated temperatures.

It is worth mentioning that the strain response of the surface chemistry and the electronic structure on the herein-reported LSC thin films is qualitatively similar to our recent findings on LSM,³⁶ while here these effects have been more systematically probed and analyzed as a function of temperature, precisely pointing to the transition temperatures and mechanisms governing the changes in electronic and chemical state on the surfaces. The electronic and ionic properties of LSM and LSC as SOFC cathodes vastly differ, the former being an ion conduction-limited oxide cathode² and the latter a surface exchange-limited one.⁸⁰ Interestingly, these differently treated perovskite oxides respond qualitatively similarly to strain in terms of the surface Sr segregation, oxygen vacancy formation, as well as electronic structure transitions at elevated temperatures. The qualitative similarity between the strain-response of LSC and LSM may render our mechanistic results discussed here applicable for describing the strain-stimulated behavior of a wider family of transition metal perovskite oxides.

4. SUMMARY AND CONCLUSION

In summary, we showed that the surface electronic and chemical state of epitaxial La_{0.8}Sr_{0.2}CoO₃ thin films varied over a range of temperatures, and the extent of this variation depended on the strain state of the films. Chemically, both the tensile strained LSC/STO and the compressively strained LSC/LAO showed Sr-rich surfaces, with slightly more Sr surface enrichment on LSC/STO. We discovered a transition from a semiconducting (energy gap) to a metallic-like state (no energy gap) on both films at ~200–300 °C, with a more enhanced DOS near the Fermi level on the LSC/STO surface for up to 450 °C in 10⁻³ mbar oxygen. The transition to the metallic-like state, and the relatively higher enhancement of DOS on the LSC/STO, is most likely due to the formation of oxygen vacancies that may induce states in the energy gap in a delocalized manner at elevated temperatures. Our DFT calculations and Co 2p photoelectron spectra indicate a lower vacancy formation energy and enhanced formation of surface oxygen vacancy defects, respectively, on LSC/STO, supporting the increased DOS near the Fermi level found from tunneling spectroscopy. We believe our results on LSC are descriptive of the strain-response of the wider family of perovskite oxides. Because the semiconducting-to-metallic transition is *reversible*, it is impossible to capture it by *ex situ* electronic structure measurements alone, underscoring the importance of the *in situ* measurement capabilities. These results represent an initial set of *in situ* correlations of the chemical and electronic state to the temperature and strain state on transition metal oxide cathodes. Further in-depth probing and analysis of such correlations on a broader range of materials and conditions are essential toward advancing our understanding of how the surface state relates to the oxygen reduction activity on SOFC cathodes and other oxides functioning at high temperatures.

■ ASSOCIATED CONTENT

S Supporting Information. Figure S1, X-ray diffraction reciprocal space map of LSC/STO and LSC/LAO thin films measured at room temperature; Figure S2, X-ray photoelectron spectra of the Sr 3d region for the cleaned surfaces of tensile strained LSC on STO and compressively strained LSC on LAO; Figure S3, tunneling current versus bias data taken on LSC/STO and LSC/LAO thin film surfaces at room temperature, 300, and 450 °C; and

Figure S4, Co 2p X-ray photoelectron spectra on the LSC/LAO film annealed at 450 °C for a prolonged time. This material is available free of charge via the Internet at <http://pubs.acs.org>.

AUTHOR INFORMATION

Corresponding Author

byildiz@mit.edu

ACKNOWLEDGMENT

We thank the US—DOE Basic Energy Sciences for financial support (Grant No. DE-SC0002633), the National Science Foundation for computational support through the TeraGrid Advanced Support Program (Grant No. TG-ASC090058), and Prof. C. Ross and Prof. H. L. Tuller at MIT for the use of their PLD system.

REFERENCES

- (1) Steele, B. C. H.; Heinzel, A. *Nature* **2001**, *414*, 345.
- (2) Adler, S. B. *Chem. Rev.* **2004**, *104*, 4791.
- (3) Jacobson, A. J. *Chem. Mater.* **2009**, *22*, 660.
- (4) Chroneos, A.; Yildiz, B.; Tarancon, A.; Parfitt, D.; Kilner, J. A. *Energy Environ. Sci.* **2011**, *4*, 2774.
- (5) Katsiev, K.; Yildiz, B.; Balasubramaniam, K.; Salvador, P. A. *Appl. Phys. Lett.* **2009**, *95*, 092106.
- (6) Yildiz, B.; Myers, D. J.; Carter, J. D.; Chang, K.-C.; You, H. *Advances in Solid Oxide Fuel Cells III: Ceramic and Engineering Science Proceedings*; John Wiley & Sons, Inc.: New York, 2009.
- (7) Fister, T. T.; Fong, D. D.; Eastman, J. A.; Baldo, P. M.; Highland, M. J.; Fuoss, P. H.; Balasubramaniam, K. R.; Meador, J. C.; Salvador, P. A. *Appl. Phys. Lett.* **2008**, *93*, 151904/1.
- (8) Estrade, S.; Rebled, J. M.; Arbiol, J.; Peiro, F.; Infante, I. C.; Herranz, G.; Sanchez, F.; Fontcuberta, J.; Cordoba, R.; Mendis, B. G.; Bleloch, A. L. *Appl. Phys. Lett.* **2009**, *95*, 173108.
- (9) Estrade, S.; Arbiol, J.; Peiro, F.; Infante, I. C.; Sanchez, F.; Fontcuberta, J.; de la Pena, F.; Walls, M.; Colliex, C. *Appl. Phys. Lett.* **2008**, *93*, 063112.
- (10) Estrade, S.; Arbiol, J.; Peiro, F.; Abad, L.; Laukhin, V.; Balcells, L.; Martinez, B. *Appl. Phys. Lett.* **2007**, *91*, 123107.
- (11) Lussier, A.; Dvorak, J.; Stadler, S.; Holroyd, J.; Liberati, M.; Arenholz, E.; Ogale, S. B.; Wu, T.; Venkatesan, T.; Idzerda, Y. U. *Thin Solid Films* **2008**, *516*, 880.
- (12) Kushima, A.; Yip, S.; Yildiz, B. *Phys. Rev. B* **2010**, *82*, 115435.
- (13) Rata, A. D.; Herklotz, A.; Nenkov, K.; Schultz, L.; Dörr, K. *Phys. Rev. Lett.* **2008**, *100*, 076401.
- (14) Kushima, A.; Yildiz, B. *J. Mater. Chem.* **2010**, *20*, 4809.
- (15) Garcia-Barriocanal, J.; Rivera-Calzada, A.; Varela, M.; Sefrioui, Z.; Iborra, E.; Leon, C.; Pennycook, S. J.; Santamaría, J. *Science* **2008**, *321*, 676.
- (16) Schichtel, N.; Korte, C.; Hesse, D.; Janek, J. *Phys. Chem. Chem. Phys.* **2009**, *11*, 3043.
- (17) Sankaranarayanan, S. K. R. S.; Ramanathan, S. *J. Chem. Phys.* **2011**, *134*, 064703.
- (18) Sanna, S.; Esposito, V.; Tebano, A.; Licoccia, S.; Traversa, E.; Balestrino, G. *Small* **2010**, *6*, 1863.
- (19) de Smit, E.; van Schooneveld, M. M.; Cinquini, F.; Bluhm, H.; Sautet, P.; de Groot, F. M. F.; Weckhuysen, B. M. *Angew. Chem.-Int. Ed.* **2011**, *50*, 1584.
- (20) Somorjai, G. A.; Frei, H.; Park, J. Y. *J. Am. Chem. Soc.* **2009**, *131*, 16589.
- (21) Lira, E.; Wendt, S.; Huo, P.; Hansen, J. Ø.; Streber, R.; Porsgaard, S.; Wei, Y.; Bechstein, R.; Lægsgaard, E.; Besenbacher, F. *J. Am. Chem. Soc.* **2011**, *133*, 6529.
- (22) Januschewsky, J.; Ahrens, M.; Opitz, A.; Kubel, F.; Fleig, J. *Adv. Funct. Mater.* **2009**, *19*, 3151.
- (23) Calle-Vallejo, F.; Martinez, J. I.; Garcia-Lastra, J. M.; Mogensen, M.; Rossmeisl, J. *Angew. Chem.-Int. Edit.* **2010**, *49*, 7699.
- (24) Sase, M.; Yashiro, K.; Sato, K.; Mizusaki, J.; Kawada, T.; Sakai, N.; Yamaji, K.; Horita, T.; Yokokawa, H. *Solid State Ion.* **2008**, *178*, 1843.
- (25) la O, G. J.; Ahn, S. J.; Crumlin, E.; Oriksa, Y.; Biegalski, M. D.; Christen, H. M.; Shao-Horn, Y. *Angew. Chem., Int. Ed.* **2010**, *49*, 5344.
- (26) Donner, W.; Chen, C.; Liu, M.; Jacobson, A. J.; Lee, Y.-L.; Gadre, M.; Morgan, D. *Chem. Mater.* **2011**, *23*, 984.
- (27) Mavrikakis, M.; Hammer, B.; Norskov, J. K. *Phys. Rev. Lett.* **1998**, *81*, 2819.
- (28) Wintterlin, J.; Zambelli, T.; Trost, J.; Greeley, J.; Mavrikakis, M. *Angew. Chem., Int. Ed.* **2003**, *42*, 2850.
- (29) Strasser, P.; Koh, S.; Anniyev, T.; Greeley, J.; More, K.; Yu, C.; Liu, Z.; Kaya, S.; Nordlund, D.; Ogasawara, H.; Toney, M. F.; Nilsson, A. *Nat Chem* **2010**, *2*, 454.
- (30) *NIST Database 82*, U.S. Department of Commerce, 2001.
- (31) Perdew, J. P.; Chevary, J. A.; Vosko, S. H.; Jackson, K. A.; Pederson, M. R.; Singh, D. J.; Fiolhais, C. *Phys. Rev. B* **1992**, *46*, 6671.
- (32) Blöchl, P. E. *Phys. Rev. B* **1994**, *50*, 17953.
- (33) Wang, L.; Maxisch, T.; Ceder, G. *Phys. Rev. B* **2006**, *73*, 195107.
- (34) Kushima, A.; Yip, S.; Yildiz, B. *Phys. Rev. B* **2010**, *82*, 115435/1.
- (35) Han, J. W.; Yildiz, B. *J. Mater. Chem.* **2011**, DOI: 10.1039/c1jm12830b.
- (36) Jalili, H.; Han, J. W.; Kuru, Y.; Cai, Z.; Yildiz, B. *J. Phys. Chem. Lett.* **2011**, *2*, 7.
- (37) Lee, Y.-L.; Kleis, J.; Rossmeisl, J.; Morgan, D. *Phys. Rev. B* **2009**, *80*, 224101.
- (38) Mastrikov, Y. A.; Merkle, R.; Heifets, E.; Kotomin, E. A.; Maier, J. *J. Phys. Chem. C* **2010**, *114*, 3017.
- (39) Chase, M. W., Jr. *NIST-JANAF Thermochemical Tables*, 4th ed.; Monograph 9; American Institute of Physics: St. Louis, MO, 1998.
- (40) Brundle, C. R. E.; Charles, A. Jr.; Wilson, S. *Encyclopedia of Materials Characterization—Surfaces, Interfaces, Thin Films*; Elsevier: New York, 1992.
- (41) Jiang, S. *J. Solid State Electrochem.* **2007**, *11*, 93.
- (42) Sharma, V. I.; Yildiz, B. *J. Electrochem. Soc.* **2010**, *157*, B441.
- (43) Dulli, H.; Dowben, P. A.; Liou, S. H.; Plummer, E. W. *Phys. Rev. B* **2000**, *62*, R14629.
- (44) Stamenkovic, V.; Mun, B. S.; Mayrhofer, K. J. J.; Ross, P. N.; Markovic, N. M.; Rossmeisl, J.; Greeley, J.; Nørskov, J. K. *Angew. Chem., Int. Ed.* **2006**, *45*, 2897.
- (45) Hammer, B.; Nørskov, J. K. *Surf. Sci.* **1995**, *343*, 211.
- (46) Feibelman, P. J.; Hamann, D. R. *Phys. Rev. Lett.* **1984**, *52*, 61.
- (47) *Theoretical Surface Science: A Microscopic Perspective*; 2nd ed.; Groß, A., Ed.; Springer Verlag: Berlin, 2009.
- (48) Mineshige, A.; Kobune, M.; Fujii, S.; Ogumi, Z.; Inaba, M.; Yao, T.; Kikuchi, K. *J. Solid State Chem.* **1999**, *142*, 374.
- (49) Tokura, Y. *Rep. Prog. Phys.* **2006**, *69*, 797.
- (50) Dagotto, E.; Hotta, T.; Moreo, A. *Phys. Rep.-Rev. Sec. Phys. Lett.* **2001**, *344*, 1.
- (51) Dorr, K. *J. Phys. D: Appl. Phys.* **2006**, *39*, R125.
- (52) Lu, Y. F.; Klein, J.; Herbstritt, F.; Philipp, J. B.; Marx, A.; Gross, R. *Phys. Rev. B* **2006**, *73*, 184406.
- (53) Ziese, M.; Semmelhack, H. C.; Han, K. H. *Phys. Rev. B* **2003**, *68*, 134444.
- (54) Fuchigami, K.; Gai, Z.; Ward, T. Z.; Yin, L. F.; Snijders, P. C.; Plummer, E. W.; Shen, J. *Phys. Rev. Lett.* **2009**, *102*, 066104.
- (55) Liang, Y.; Bonnell, D. A. *Surf. Sci.* **1994**, *310*, 128.
- (56) Marsh, H. L.; Deak, D. S.; Silly, F.; Kirkland, A. I.; Castell, M. R. *Nanotechnology* **2006**, *17*, 3543.
- (57) Tanaka, H.; Matsumoto, T.; Kawai, T.; Kawai, S. *Jpn. J. Appl. Phys.* **1993**, *32*, 1405.
- (58) Chen, Y.; Chung, W.; Tuller, H.; Yildiz, B. Manuscript in preparation, 2011.
- (59) Szot, K.; Speier, W.; Carius, R.; Zastrow, U.; Beyer, W. *Phys. Rev. Lett.* **2002**, *88*, 075508/1.
- (60) Senarisrodriguez, M. A.; Goodenough, J. B. *J. Solid State Chem.* **1995**, *118*, 323.

- (61) Feng, Z.; Kim, C.-Y.; Elam, J. W.; Ma, Q.; Zhang, Z.; Bedzyk, M. *J. Am. Chem. Soc.* **2009**, *131*, 18200.
- (62) Horita, T.; Ishikawa, M.; Yamaji, K.; Sakai, N.; Yokokawa, H.; Dokiya, M. *Solid State Ion.* **1998**, *108*, 383.
- (63) Senarisrodriguez, M. A.; Goodenough, J. B. *J. Solid State Chem.* **1995**, *116*, 224.
- (64) Mizusaki, J.; Mima, Y.; Yamauchi, S.; Fueki, K.; Tagawa, H. *J. Solid State Chem.* **1989**, *80*, 102.
- (65) Szot, K.; Speier, W.; Carius, R.; Zastrow, U.; Beyer, W. *Phys. Rev. Lett.* **2002**, *88*, 075508.
- (66) Diebold, U.; Li, S. C.; Schmid, M. In *Annual Review of Physical Chemistry*; Annual Reviews: Palo Alto, 2010; Vol. 61, p 129.
- (67) Bertel, E.; Stockbauer, R.; Madey, T. E. *Phys. Rev. B* **1983**, *27*, 1939.
- (68) Di Valentin, C.; Pacchioni, G.; Selloni, A. *Phys. Rev. Lett.* **2006**, *97*, 166803.
- (69) Kim, Y. S.; Kim, J.; Moon, S. J.; Choi, W. S.; Chang, Y. J.; Yoon, J. G.; Yu, J.; Chung, J. S.; Noh, T. W. *Appl. Phys. Lett.* **2009**, *94*, 202906.
- (70) Ganduglia-Pirovano, M. V.; Hofmann, A.; Sauer, J. *Surf. Sci. Rep.* **2007**, *62*, 219.
- (71) Africh, C.; Köhler, L.; Esch, F.; Corso, M.; Dri, C.; Bucko, T.; Kresse, G.; Comelli, G. *J. Am. Chem. Soc.* **2009**, *131*, 3253.
- (72) Rodriguez, J. A.; Jirsak, T.; Liu, G.; Hrbek, J.; Dvorak, J.; Maiti, A. *J. Am. Chem. Soc.* **2001**, *123*, 9597.
- (73) König, T.; Simon, G. H.; Rust, H. P.; Pacchioni, G.; Heyde, M.; Freund, H. J. *J. Am. Chem. Soc.* **2009**, *131*, 17544.
- (74) Vaz, C. A. F.; Prabhakaran, D.; Altman, E. I.; Henrich, V. E. *Phys. Rev. B* **2009**, *80*, 155457.
- (75) Petitto, S. C.; Marsh, E. M.; Carson, G. A.; Langell, M. A. *J. Mol. Catal. A-Chem.* **2008**, *281*, 49.
- (76) Kim, J. G.; Pugmire, D. L.; Battaglia, D.; Langell, M. A. *Appl. Surf. Sci.* **2000**, *165*, 70.
- (77) Rodriguez, J. A.; Hanson, J. C.; Frenkel, A. I.; Kim, J. Y.; Pérez, M. *J. Am. Chem. Soc.* **2001**, *124*, 346.
- (78) Lindsay, R.; Michelangeli, E.; Daniels, B. G.; Ashworth, T. V.; Limb, A. J.; Thornton, G.; Gutiérrez-Sosa, A.; Baraldi, A.; Larciprete, R.; Lizzit, S. *J. Am. Chem. Soc.* **2002**, *124*, 7117.
- (79) Gong, X.-Q.; Selloni, A.; Dulub, O.; Jacobson, P.; Diebold, U. *J. Am. Chem. Soc.* **2007**, *130*, 370.
- (80) Baumann, F. S.; Fleig, J.; Habermeier, H.-U.; Maier, J. *Solid State Ion.* **2006**, *177*, 1071.